ACCSCIENCE PUBLISHING

International Journal of Bioprinting

RESEARCH ARTICLE

Multimaterial vat photopolymerization: Computational optimization of slicing workflow for complex tissue geometries

Alejandro González-Santos[1], Adrian García[2], Nadina Usseglio[2], Julián Flores[1], and Daniel Nieto[2,3]*

[1]Department of Electronics and Computing, University of Santiago de Compostela. Santiago de Compostela, Galicia, Spain.

[2]Advanced Biofabrication Laboratory (DNIETO Lab), Interdisciplinary Center for Chemical and Biology, Universidade da Coruña, A Coruña, Galicia, Spain.

[3]Oportunius Program, Axencia Galega de Innovación, Santiago de Compostela, Galicia, Spain

Abstract

Multimaterial printing using digital light processing (DLP) has progressed from a niche laboratory method to a scalable technology capable of fabricating complex and functional tissue constructs. However, current multimaterial DLP workflows face significant limitations. Material changes typically require repeated washing and reloading steps, which increase print time, raise the risk of cross-contamination or layer misalignment, and ultimately constrain scaffold design complexity and biological relevance. To address these challenges, we present a computational pipeline that significantly improves the efficiency, precision, and usability of DLP for multimaterial bioprinting. Our system includes three key innovations: (i) a high-resolution segmentation and material-labeling method using computer graphics techniques for accurate material assignment in Standard Tessellation Language (STL) models; (ii) a computer vision-based algorithm for real-time detection and correction of material interference or contamination; and (iii) a GPU-accelerated layer sequencing method that supports rapid, precise material switching within single-layer projections. Experimental validation demonstrates improved print fidelity, reduced processing time, and higher material resolution. We further showcase the practical utility of our system by bioprinting a multimaterial tissue construct composed of a poly(ethylene glycol) diacrylate-based scaffold integrated with a gelatin methacryloyl-based cell-laden microenvironment. This work represents a significant step toward enabling scalable, high-resolution, and biologically functional scaffold fabrication for advanced tissue engineering applications.

Keywords: 3D printing protocol; Multimaterial digital light processing printer; Process planning algorithm; Slicing

***Corresponding author:**
Daniel Nieto
(daniel.nieto@udc.es)

Citation: González-Santos A, García A, Usseglio N, Flores J, Nieto D. Multimaterial vat photopolymerization: Computational optimization of slicing workflow for complex tissue geometries. *Int J Bioprint*. 2026;12(1):523-539. doi: 10.36922/IJB025470480

Received: November 18, 2025
Revised: December 12, 2025
Accepted: December 16, 2025
Published online: December 19, 2025

1. Introduction

Three-dimensional (3D) bioprinting has emerged as a transformative technology for fabricating biological structures. This field leverages additive manufacturing principles to create complex, cell-laden tissues with precise spatial arrangements.[1] Recent advances

in bioprinting techniques and biomaterials have opened new possibilities for developing transplantable tissues, including vascular grafts, bone, cartilage, and cardiac structures.[2,3] However, the fabrication of fully functional organs remains an ongoing challenge, as current bioprinting methods struggle to replicate the intricate microstructures and physiological complexity of human tissues.[4]

Light-based bioprinting technologies are a subset of 3D bioprinting methods that utilize light to precisely pattern and solidify bioinks containing living cells and biomaterials. Among them, vat photopolymerization (VPP) is an additive manufacturing technology in which a liquid photosensitive resin is selectively solidified layer by layer using a controlled light source. The primary techniques include stereolithography (SLA)[5] and digital light processing (DLP).[6] In SLA, a focused UV laser scans the surface of the resin, curing the material point by point to build each layer with very high precision and smooth surface quality. In DLP, an entire layer is cured at once by exposing the bioink to light patterns using a digital micromirror device, allowing for faster fabrication while maintaining precision. Both techniques enable the production of detailed, accurate parts. However, SLA excels in surface finish and fine features, whereas DLP stands out for its ability to produce high-resolution tissue structures with scalable fabrication capabilities using photosensitive bioinks. While the DLP process can be highly precise, it requires careful control of factors such as ink surface levels, material purity, and biomaterial management.[6]

While early applications typically relied on monomaterial printing due to its simplicity, the limitations of this approach became apparent as the need arose to recreate structures containing different cell types and structural matrices. The transition to multimaterial manufacturing represents a significant advance, focusing on optimizing not only the performance of the printing process but also the morphological and functional qualities of the resulting structure.[7]

The slicing strategies used in DLP bioprinting remain largely planar and uniform, which limits the ability to fabricate anatomically accurate or functionally graded tissues. Although adaptive and non-planar slicing algorithms have been proposed, their integration into DLP systems is challenging due to hardware constraints and a lack of standardized, user-friendly software.[8] In addition, most DLP platforms operate in an open-loop mode, meaning they cannot compensate for dynamic changes during printing—such as thermal expansion and the settling of bioinks—which can lead to geometric distortions or layer delamination. While real-time imaging techniques (e.g., optical coherence tomography and fluorescence monitoring) have been explored for feedback control,[9] incorporating these into DLP systems remains technically complex and cost-prohibitive for most laboratories. This is particularly important when manufacturing objects composed of multiple materials, as efficient material management becomes crucial for success. For example, Kim *et al.*[10] proposed an algorithm to optimize material transitions in DLP bioprinting, reducing the need for frequent cleaning and leveling during material changes. Segmenting and converting this data into printable models without introducing artifacts or compromising resolution is non-trivial, and current slicing tools often lack the sophistication to preserve biologically relevant features.

Some researchers have previously reported multimaterial VPP strategies for 3D printing. Shaukat *et al.*[11] categorized the principal strategies into: (i) sequential resin–vat exchange, (ii) in-vat selective activation via dual-wavelength or graded doses, and (iii) dual-curing or multi-reaction systems. A recent experimental example is the dual-vat DLP implementation for vitrimers, described by Shaukat *et al.*,[12] which achieves high functional integration by physically exchanging vats during the build process. Another notable advance is the dual-wavelength VPP method reported by Chin *et al.*,[13] which enables the production of multimaterial or multi-color prints from a single resin vat by modulating photoreactions with different wavelengths. In addition, Ghaderi *et al.*[14] have demonstrated a multimaterial VPP platform based on dual vats combined with an intermediate ultrasonic cleaning station and automated vat switching, enabling efficient fabrication of complex structures such as scaffolds for bone regeneration while mitigating resin cross-contamination.

The primary objective of this study is to enhance the precision and efficiency of top–down DLP bioprinting for multimaterial, cell-laden constructs by algorithmically optimizing the slicing workflow and material change sequence, independent of major hardware modifications. By minimizing the number of material-switch events and aligning layer sequences to reduce idle or cleaning times, we directly address efficiency bottlenecks inherent in prior methods. The algorithm operates directly on a voxelized 3D model, enabling accurate layer control and reducing the number of material transitions during printing. Following theoretical validation and acellular printing tests, the system was applied to the fabrication of living tissue constructs, demonstrating high structural fidelity and good cell viability, confirming its potential for advanced biofabrication applications. The methodology is presented in **Section 2**, followed by results and discussion in **Section 3** and a conclusion in **Section 4**.

2. Materials and methods

2.1. Bioprinting system and methodology

For the work presented in this study, we utilized a custom-built DLP-based stereolithographic "top–down" 3D bioprinter designed for multimaterial bioprinting applications (Figure 1A). The system integrates several key components: a high-resolution DLP projector (Wintech PRO6600, Wintech Digital Systems Technology Corp., United States [US]) with 4K resolution (3840 × 2160 pixels), a 385 nm wavelength, and over 3000 mW power output to initiate photopolymerization; a *Z*-axis-controlled printing platform driven by a stepper motor for precise vertical positioning; a 4K-capable webcam (ELP USB4KHDR01-KL100, Shenzhen Ailipu Technology Co., Ltd., China) for real-time process monitoring and video recording; and a control computer equipped with custom software that allows coordinated operation of all components through an integrated touchscreen interface (Figure 1A).

To demonstrate the multimaterial capabilities of the developed algorithm, we designed two initial printing models: (i) a two-material lateral intersection, where distinct materials meet side by side (Figure 1Bi); and (ii) a two-material embedded configuration, where one material is printed within another (Figure 1Bii). As a more complex demonstration, we further introduced a multimaterial bioprinting model consisting of a gelatin methacryloyl (GelMA)-based, cell-laden bioink embedded within a poly(ethylene glycol) diacrylate (PEGDA)-based structural scaffold (Figure 1C).

2.2. Bioprinting workflow

2.2.1. Single material slicing

The workflow from a computer-aided design (CAD) single-material model to a real object printed with an SLA or DLP printer begins with designing the object using CAD software, followed by optimization by engineers or designers to ensure its correct manufacturability. After the model is finalized, it is exported to a file format compatible with 3D printing. The most commonly used format is STL. STL files represent the surface of the 3D model as a mesh of interconnected triangles. This file format captures the geometry but does not include color, texture, and material properties. Then, the STL file is loaded into slicing software tailored for SLA/DLP printers. The slicer generates a layer-by-layer representation of the object, along with other process parameters, such as exposure time and the

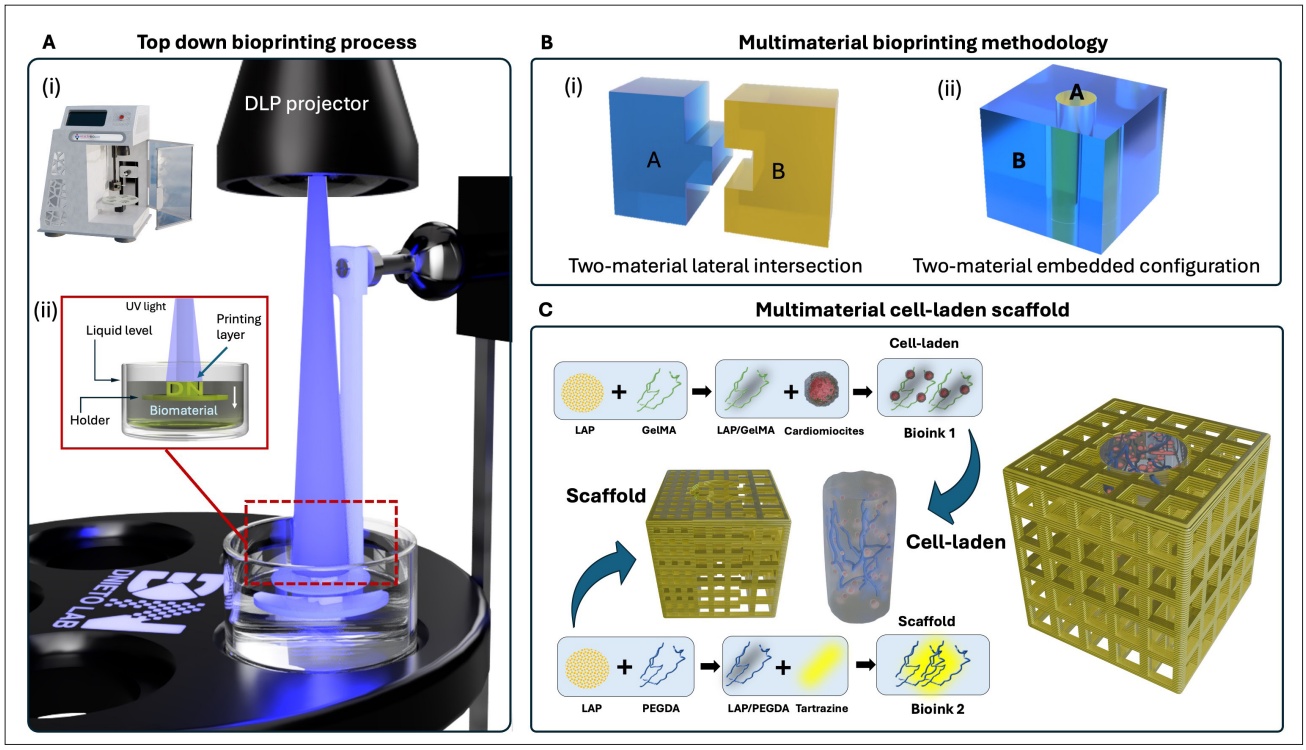

Figure 1. Overview of the top–down multimaterial DLP bioprinting platform and workflow enabled by the proposed algorithm. (A) Top–down bioprinting process: (i) the bioprinter and (ii) schematic of the working chamber. (B) Multimaterial bioprinting configurations used to demonstrate the capabilities of the proposed algorithm: (i) a two-material lateral intersection and (ii) a two-material embedded configuration. (C) Multimaterial cell-laden scaffold bioprinting workflow. Abbreviations: DLP: digital light processing; GelMA; gelatin methacryloyl; LAP: lithium phenyl-2,4,6-trimethylbenzoylphosphinate; PEGDA: poly(ethylene glycol) diacrylate.

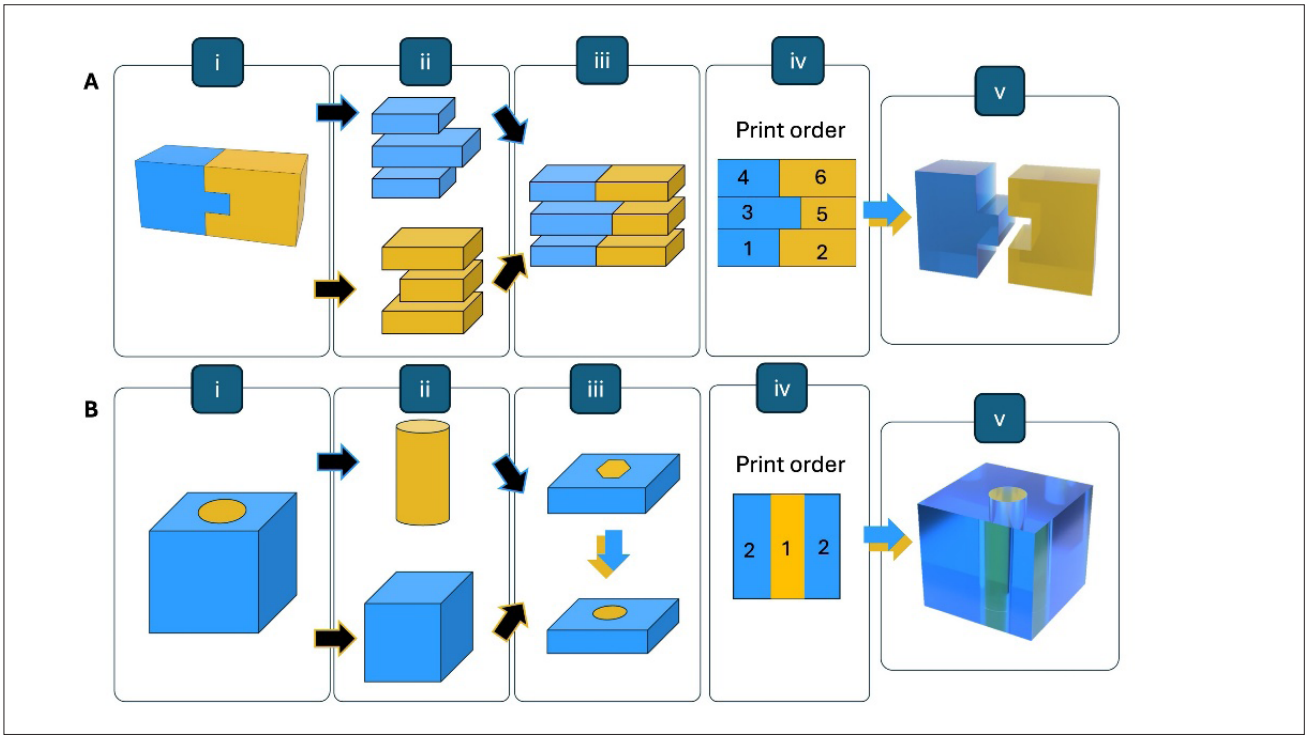

Figure 2. Overview of the digital light processing printing workflow for multimaterial objects using the (A) intersection and (B) enclosed configurations: (i) virtual object, (ii) conversion of the virtual object to a standard tessellation language (STL) model, (iii) generation and verification of sliced images from the STL model, (iv) determination of printing order, and (v) projection of the images to fabricate the physical objects.

intensity of the laser or DLP projector. The slicing software provides a layer-by-layer preview to inspect the object for errors, such as missing supports or incomplete layers. It must inform the user of any problems or potential artifacts that may occur. This step must ensure the file is ready for printing (Figure 2).

Once the printer is prepared, the printing process is initiated. The printer creates the object layer by layer, image by image, by curing the ink using a DLP projector that displays a full slice of the layer simultaneously. Each image is a single layer, whose thickness is determined by the user, and its combination will be the final physical object.

2.2.2. Multimaterial slicing

The manufacturing of a multimaterial object using a DLP 3D printer differs from that of a single-material object, as it involves solving several challenges. The first of these challenges is directly associated with the use of STL files for representation, as the STL format represents the surface of an object as a mesh of triangles and does not include material properties; it only defines the geometry. Therefore, the primary issue is how to identify and differentiate each material within an STL file. Since the format lacks the capability to encode material information, alternative approaches must be developed, such as using multiple STL files (one for each material) or adopting more advanced file formats like OBJ, 3MF, or AMF, which support multimaterial representation. Some printers use custom software to identify materials within a model; however, the most widely adopted solution for fused deposition modeling printers is dividing the model into several STL files and assigning each material to a separate file. This approach does not pose any issues for end users, as most CAD software allows for splitting models, selecting independent parts, and exporting them as separate STL files.

Another challenge in the tessellation of multimaterial 3D objects into triangular meshes is the introduction of approximation errors. This issue is particularly pronounced in organic shapes, which are defined by complex curvatures rather than planar surfaces. These problems arise during the triangulation process, when two closely spaced curved elements are discretized or even within a single object featuring proximate surfaces, the resulting facets may intersect, despite the original geometries being non-intersecting (Figure 3). In these cases, the boundaries between different materials are often spatially coincident or separated by a negligible distance. The subsequent mesh intersections represent a critical failure mode for 3D printing, as they lead to ambiguous material boundaries

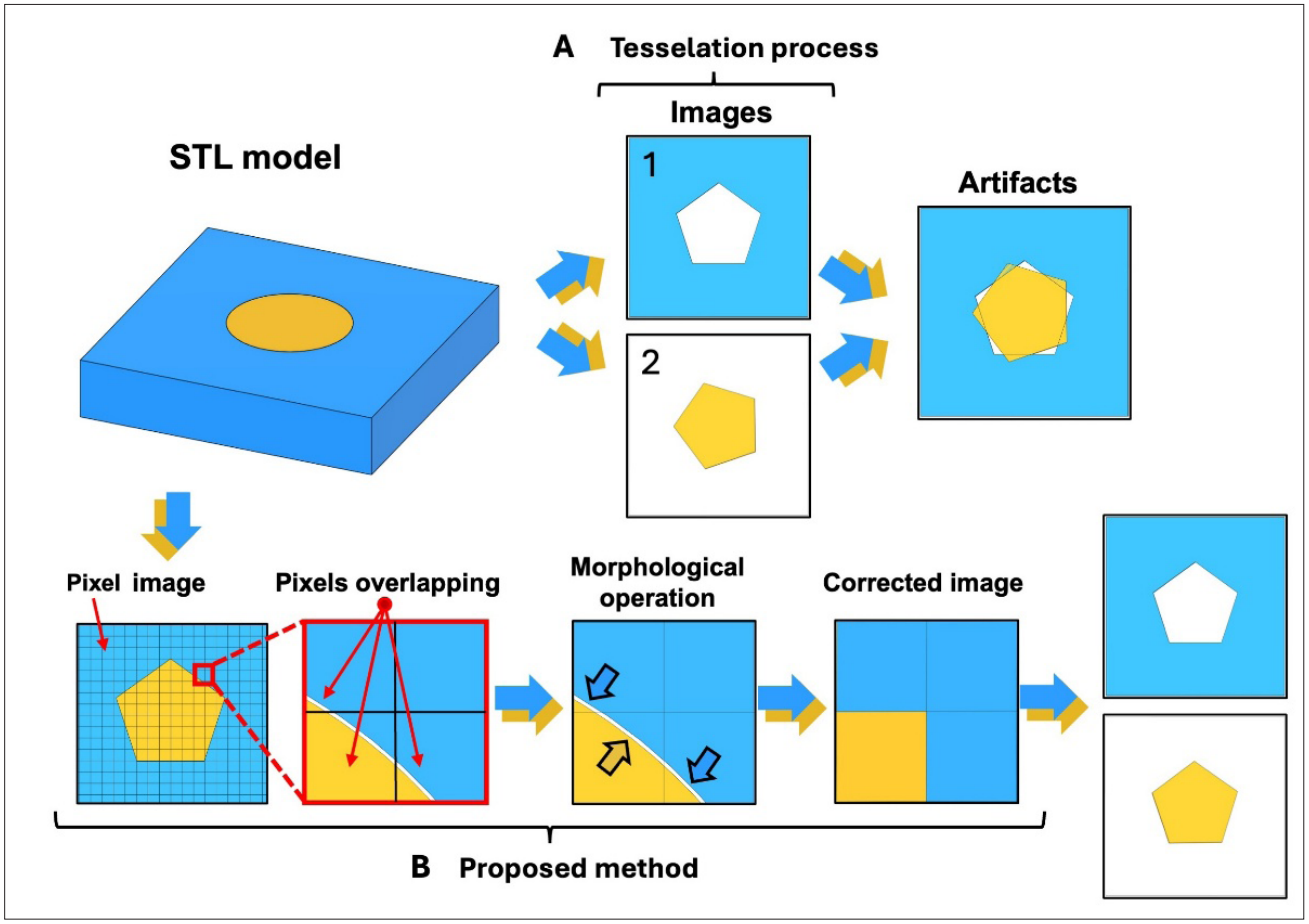

Figure 3. Identification and correction of tessellation-induced artifacts in multimaterial STL representations. (A) Two-material object tessellations showing artifacts introduced during triangulation and their superposition in the final image representation. (B) Standard tessellation approximation (top) and corresponding morphological correction (bottom). Abbreviation: STL: Standard Tessellation Language.

and processing errors. Consequently, the fabrication of multimaterial objects is complicated, necessitating meticulous mesh repair, stringent alignment tolerances, or the use of specialized file formats and software tools to ensure non-interfering material geometries.[15]

2.3. Slicing algorithm and workflow

The process workflow, illustrated in Figure 2, comprises four key stages: first, the multimaterial STL model is decomposed into distinct single-material sub-models; second, the printing layers for each sub-model are generated; third, a geometric analysis is performed to identify and resolve inter-layer intersections arising from tessellation; and finally, a topological optimization of the layer sequence is conducted to consolidate printing phases, thereby preventing bioink accumulation and minimizing washing cycles. The initial step involves separating the multimaterial object into its constituent parts, with each component exported as an individual STL file. Although our custom-developed software was used for this separation procedure, conventional slicing platforms such as Chitubox, Lychee Slicer, and NanoDLP, as well as standard CAD software, are equally suitable. Subsequently, these files are sliced independently, generating a distinct set of images for each material (Figure 3, Step 2). Once separated, each STL file undergoes the slicing process, generating the set of images required to print each material part of the objects. The number of images depends on the object's size and the layer height selected for the print.

For the slicing, we used the computer graphics algorithm described by Keeter.[16] The slicing process begins by dividing the input STL model into layers of a user-defined thickness. The core challenge is then to determine which regions of each layer constitute the solid object. To solve this, each layer is discretized into a grid of voxels, where each voxel corresponds to a pixel in the image of each layer. For each voxel/pixel, a ray is cast from outside the object's bounding volume until the height of the layer that is to be printed. The number of intersections of a ray with the model's triangles

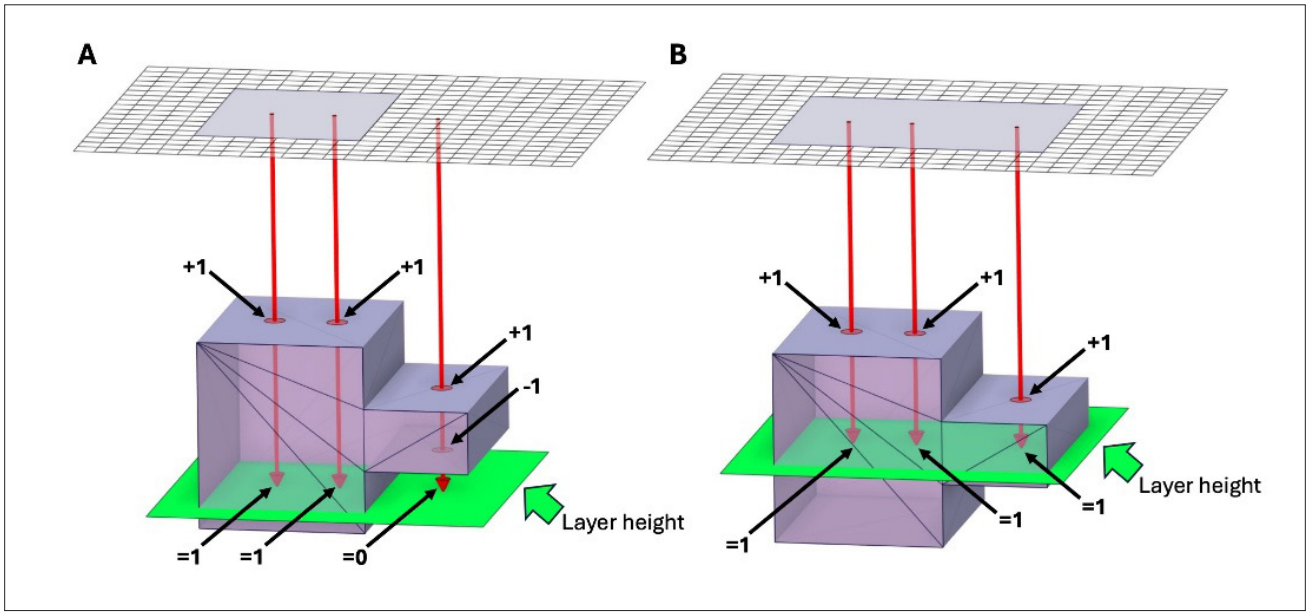

Figure 4. Ray-casting algorithm.[16] (A) Four rays cast from the screen pass through the object once, up to the layer height, corresponding to filled pixels in the image. (B) The third ray enters the object (+1) and exits (−1), resulting in a net value of 0, which corresponds to an empty pixel in the image for that layer.

is counted using a winding-order rule: an intersection with a front-facing triangle increments a counter, while an intersection with a back-facing triangle decrements it. A final count greater than zero indicates the voxel is inside the solid, and therefore the pixel must be set to on (Figure 4). This logic is efficiently implemented on the GPU via a stencil buffer[17] technique in three rendering passes: the buffer is first incremented on front-facing fragments, then decremented on back-facing ones, and finally, only pixels with a positive value are preserved. This approach executes the insideness test in a massively parallel manner, effectively offloading the complex computational burden of intersection detection from the Central Processing Unit (CPU) to the Graphics Processing Unit (GPU).

Once the object is divided into material-specific layers, the previously mentioned approximation errors (intralayer errors) from triangulation can be analyzed (Figure 3, Steps 3 & 4; and Figure 5). In our case, since the models were sliced into independent sets of images, these approximation errors manifested as image overlapping issues. These problems were easy to detect, as we only needed to perform a Boolean operation to assess whether the same pixel was assigned to more than one layer of one material. These phantom overlaps were removed using a morphological erosion operation on the images (Figure 3B).[18] The radius for this operation is derived from a user-defined tolerance parameter, and a new validation check ensures that each pixel contains at most one material. In other words, it is guaranteed that a pixel will never be occupied by more than one material. If the overlap cannot be corrected, the process is aborted, and the user is notified of the issue. The software then allows the user to either increase the tolerance parameter or review the STL models before proceeding with the printing process. This method aligns more closely with the intrinsic operation of the DLP projection device by working at the pixel level, thereby avoiding purely geometric operations. Consequently, in the event of modifications to the device, such as an increase in its resolution, the adjustment process would be significantly more straightforward. With this step, we obtained the final set of images and arranged them correctly for projection.

2.4. Problem statement

Once the models were processed into sets of slices, we determined the order in which those slices would be printed. As mentioned in the introduction, the order significantly impacts the efficiency of the printing process. The platform must then be aligned with the surface of the previously printed slice of the same material, taking into account the ink's surface and the offset between layers.

Therefore, the ideal approach would be to print each layer of material sequentially, starting from the bottom and moving to the top, followed by all layers of the second material, and so on, until all layers of every material are printed. However, certain physical constraints in the printing process make this optimal plan unfeasible for some 3D shapes:

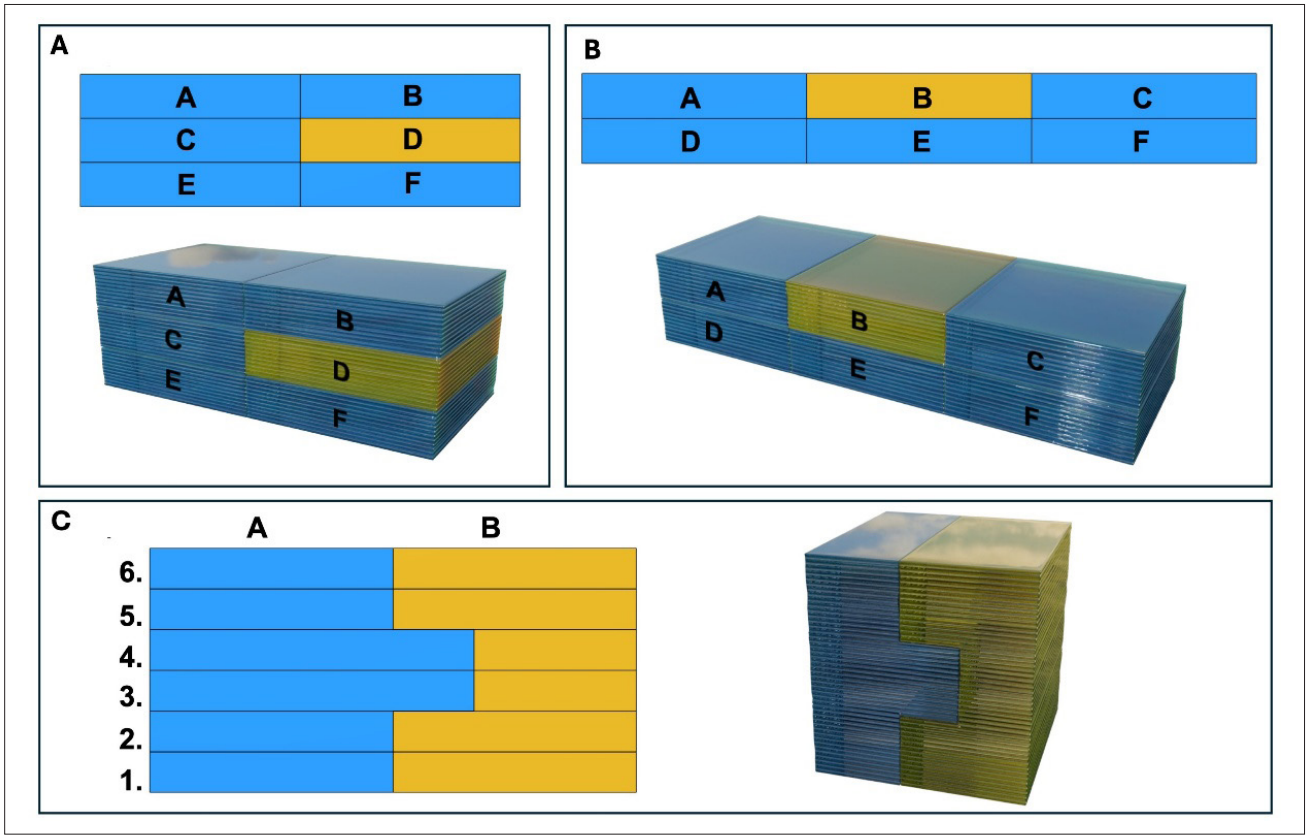

Figure 5. Examples of objects in which the identified constraints apply (side view): (A) Overlapping materials: segment B cannot be printed before segment D, requiring a material change after segment C is printed; (B) Trapped ink: segment B must be printed before segments A and C; otherwise, uncured ink of the orange material would be trapped inside B; (C) Additional example of overlapping materials: material B of layer 2 must be printed before material A of layer 3, and material A of layer 4 must be printed before material B of layer 5.

- If a layer of one material is placed directly on top of another layer of a different material (Figure 5A), the bottom layer must be printed first. Otherwise, the upper layer would block the light from reaching the lower one, making printing impossible.
- If a layer of one material completely encloses a layer of a different material at the same height, the inner layer must be printed first. Otherwise, the outer layer would trap the ink inside (Figure 5B), preventing it from being replaced by the new material's ink. A more aggressive cleaning process could remove the trapped ink, but this would be wasteful if a large volume of uncured material is involved.

2.5. Algorithm

The core principle of the algorithm is to trace a ray in a given direction and divide it into smaller segments, analyzing how each segment interacts with its surrounding environment. In our most basic case, we cast a ray downward from a point in a material layer. This ray advances in steps equal to the layer's thickness, checking at each step whether it intersects or encounters a different material in another layer.

This technique offers two key advantages. First, it allows for easy topological inclusion analysis. For example, in the case of a completely enclosed material, tracing rays in multiple directions around the voxel under study is sufficient to determine whether it encounters different materials. Second, since the algorithm is efficiently implemented on a GPU, voxel evaluations can be performed in parallel, significantly accelerating the process.

It is not necessary to perform this operation for every pixel of the image. Instead, the image can be voxelized with a voxel size determined by the projector's resolution as the base and the layer height. If the image resolution is provided by the slicer, it matches the resolution of the projector, meaning that pixels and voxels have the same dimensions. However, larger images are typically used to enhance precision and reduce aliasing issues. Using this approach, we developed the following algorithm: Two 3D Boolean arrays of size $m \times n \times z$ are created, where $m \times$

n represents the number of voxels/pixels in the projected image and z corresponds to the number of slices. Every element was initialized to zero. The first array (printed pixels) stores information about voxels that have already been printed, regardless of the material. The second array (pending) contains the voxels that belong to the model but have not yet been printed, irrespective of the material. The steps of the algorithm are as follows:

1 Select the first slice of the first material and print it.

2 Pick the next unprinted layer of the currently selected material (layers of the same material are always printed sequentially, from bottom to top):

   a Apply the ray marching technique by tracing a ray from each voxel in the layer down to the bottom edge of the model. Record the index of the highest intersected layer for each material.

   b Check material dependencies:

      (i) If the highest intersected layer of a given material is above its highest printed layer, that layer must be printed first.

      (ii) Switch to that material and return to Step 2, repeating these checks for the next pending layer of the newly selected material.

   c Check for trapped uncured ink:

      (i) Extract the contour of the layer image, fill it (removing any holes), and perform a Boolean AND operation with the pending voxels of that layer.

      (ii) If the holes overlap any pending voxels, switch to the material with the most pending trapped voxels and return to Step 2.

3 Update the printing sequence:

   a Add the selected layer-material combination to the printing sequence.

   b Mark its voxels as printed in the Printed array and remove them from the Pending array.

4 Repeat until completion:

   a If there are still pending layers, return to Step 2.

   b Otherwise, the printing process is complete.

This layer-sorting algorithm aligns with the printing process by operating directly on the images to be projected, bypassing traditional geometric relationships. Furthermore, it can be fully implemented on the GPU, significantly accelerating processing speed. The ray tracing Step 2a of this algorithm requires that for each voxel in each layer under consideration, all voxels beneath it must be checked. This leads to a total of $(n-1)(n-2)$ checks per x, y position, where n is the number of layers. As a result, the algorithm has an $O(n^2)$ complexity with respect to the number of layers. This issue was addressed by introducing an auxiliary integer-valued 3D texture for each material. Each voxel in this texture stores the layer index (Z position) of the highest pending voxel below it. Therefore, to obtain the index of the highest pending voxel intersecting the ray between the voxel and the bottom of the 3D model, we only needed to read a single value from the auxiliary texture, reducing the complexity to $O(n)$ with respect to the number of layers. However, the memory usage of the required auxiliary array scales with the total number of voxels. Therefore, if the number of layers is small, the original approach might be preferable, as the performance benefits may not outweigh the increased memory consumption.

2.6. 3D printing

2.6.1. 3D design

All digital models were designed using Autodesk Fusion 2025 (Autodesk Inc., US; educational license) and exported as STL files. Three model families were created to address distinct objectives within this study: (i) PEGDA-only test structures used to assess DLP resolution/capability and to exercise the multimaterial planning logic; (ii) solid cylinders (radius 4 mm, height 6 mm) for subsequent physical characterization; and (iii) multimaterial scaffolds consisting of a square PEGDA lattice (5 × 5 × 5 mm) with gap sizes of 200, 400, or 600 μm and a concentric GelMA interior cylinder (radius 1 mm, height 5 mm). All schematic figures were created in Blender 4.5 LTS (Blender Foundation, The Netherlands), using a consistent scale across figures to maintain consistent metric dimensions.

2.6.2. 3D printing process

To evaluate the algorithm's performance in 3D printing, two bicomponent models were fabricated using a PEGDA solution with two different dyes (yellow and red). The printing parameters were set as follows: LED intensity of 21.5 mW/cm^2, exposure time of 5 s, and layer thickness of 100 μm. After each print, images of the models were captured using a magnifying lens.

2.6.3. Printing resolution assessment

To evaluate optical resolution and layer fidelity, three PEGDA lattice scaffolds (5 × 5 × 5 mm) were printed with nominal gap sizes of 200, 400, and 600 μm. The printing parameters were set as follows: LED intensity of 15.14 mW/cm^2, exposure time of 5 s, and layer thickness of 100 μm. Printed scaffolds were imaged using a Leica MATEO FL fluorescence microscope (Leica Microsystems, Germany).

2.6.4. Relationship between light exposure and material crosslinking

(a)Stiffness characterization
Cylindrical specimens (4 mm diameter, 6 mm height) were printed from 5% w/v PEGDA (molecular weight [MW] = 575 Da) containing 0.1% w/v lithium phenyl-2,4,6-trimethylbenzoylphosphinate (LAP) and 0.025% w/v tartrazine, using a layer height of 0.10 mm and the same layer exposure as above. Immediately after printing, samples were either tested as printed or subjected to a post-cure consisting of a 60 s exposure at the projector's maximum irradiance (95.83 mW/cm^2; cumulative dose 5.75 J/cm^2) while keeping the constructs hydrated. Unconfined compression tests were performed on a Mach-1 system (Biomomentum, Canada) in stress–relaxation mode at 37°C with samples submerged in phosphate-buffered saline (PBS); constructs were compressed to 40% strain at 20% speed. The apparent elastic modulus was calculated from the initial linear region of the stress–strain curve and reported as mean ± SD ($n \geq 3$ per condition).

(b) Swelling ratio
The swelling ratio (Q_M) of PEGDA constructs was evaluated to estimate crosslinking density and water uptake capacity, parameters that influence nutrient diffusion and mechanical behavior in hydrogels.[19] Disk-shaped samples were printed using the same formulation and dimensions described above. After printing and post-curing, specimens were immersed in PBS at 37°C for 24 h to reach equilibrium swelling, blotted to remove surface liquid, and weighed to obtain the swollen mass (W_s). The samples were then dried at 60°C for 48 h to obtain the dry mass (W_d). The Q_M was calculated as[20,21]:

$$Q_M = (W_s - W_d)/W_d \quad (1)$$

Measurements were performed in triplicate.

2.7. Cell bioprinting

2.7.1. Cell sourcing

Cardiomyoblasts (H9c2) were used in this study. The cells were cultured in Dulbecco's modified Eagle medium (DMEM; Gibco, US), supplemented with 10% fetal bovine serum (Capricorn Scientific, Germany) and 1% penicillin/streptomycin (Sigma-Aldrich, US), under standard culture conditions (37°C, 5% CO_2). Upon reaching approximately 80% confluence, cells were subcultured using 0.25% trypsin-ethylenediaminetetraacetic acid (Sigma-Aldrich, US).

2.7.2. Preparation of bioinks

Two bioinks were formulated: a 5% w/v PEGDA (MW = 575 Da) solution containing 0.1% w/v LAP as a photoinitiator, and 0.025% w/v tartrazine as a photoabsorber; and a 5% w/v GelMA solution with 0.1% w/v LAP. The GelMA solution was combined with an H9c2 suspension to achieve 0.7 × 10^6 cells/mL, mixing slowly at 37°C. Both solutions were prepared using DMEM as a solvent.

2.7.3. Bioprinting procedure

A multimaterial scaffold consisting of a square PEGDA lattice (5 × 5 × 5 mm) with a gap size of 200 μm and a concentric GelMA interior cylinder (radius 1 mm, height 5 mm) was designed with a layer thickness of 100 μm. The structure was divided into two by the materials that composed it. The printing parameters were set to 5 s of exposure per layer and a light intensity of 15.14 mW/cm^2. First, the PEGDA structure was printed. After printing, the structure was cleaned with Hank's Balanced Salt Solution (HBSS, Sigma Aldrich, US) to remove excess non-crosslinking material and then exposed for 60 s at 95.83 mW/cm^2 to ensure complete crosslinking of the material.

Subsequently, the printing process was continued with the GelMA cylinder containing the cell-laden bioink, and another cleaning step was performed to remove excess material. Immediately, the constructs were covered with culture medium and incubated under standard conditions (37°C, 5% CO_2) for up to 5 days. All the samples were prepared in triplicate.

2.7.4. Cell viability assay

Cell viability within the bioprinted constructs was assessed at days 1, 3, and 5 post-printing using the Live/Dead Cell Imaging Kit (Sigma-Aldrich, US). Briefly, samples were washed twice with HBSS and stained with calcein-AM, propidium iodide, and Hoechst 33342, following the manufacturer's instructions. Samples were incubated for 60 min in the dark, and fluorescence images were acquired using a fluorescence microscope (MATEO FL, Leica, Germany). Image analysis was performed using FIJI (ImageJ) software.[22]

2.8. Statistical analysis

The data collected in this work are presented as mean ± SD, and were statistically analyzed using one-way analysis of variance with GraphPad Prism (8.0.1, GraphPad Software, Inc., US). The differences were considered significant if p-values were less than 0.05.

3. Results and discussion

To validate the capabilities of the proposed algorithm, we first performed a theoretical comparison of the number of material changes and, therefore, the cleaning sequences required for three example objects using our approach compared to a naïve sequencing method. Then, we experimentally validated the method by printing

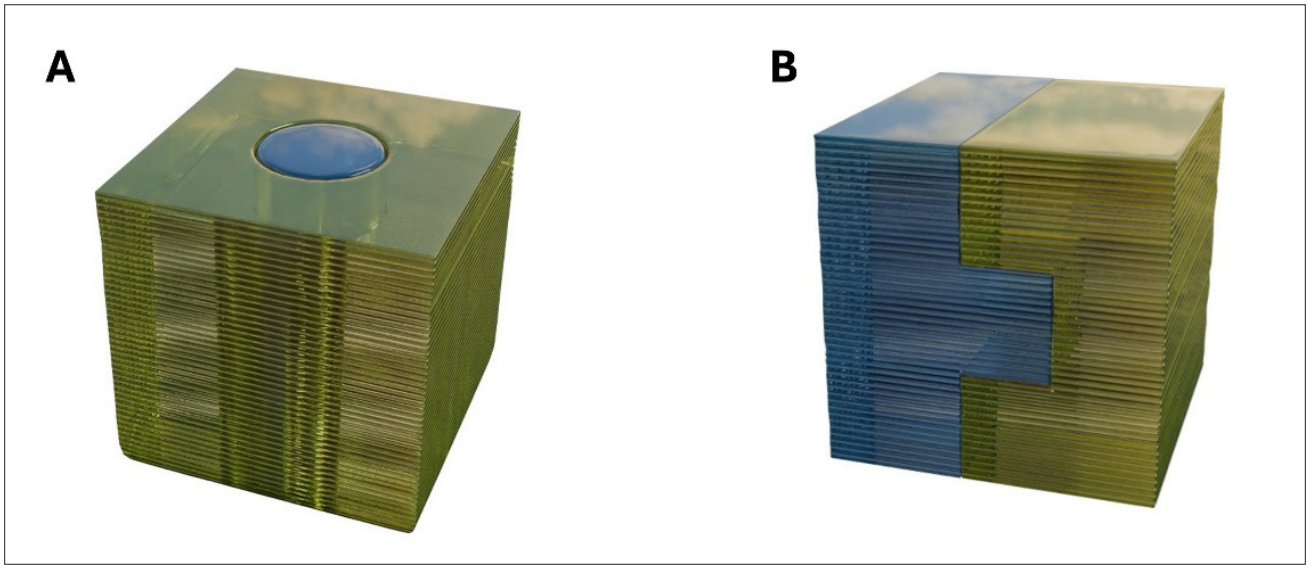

Figure 6. Models used for theoretical validation. (A) Cube with an enclosed cylinder. (B) Cube composed of two interlocking pieces.

two objects, each showcasing the previously identified challenges, and conducting a biocompatibility assessment on one of the printed structures.

3.1. Theoretical validation

The algorithm was executed on two models selected to showcase its capabilities, specifically, those with layer overlapping and ink trapping constraints described in the problem statement. The chosen models are:

(i) A cube with a cylinder of a different material enclosed in it (Figure 6A). This is an example of the trapping constraint: if the cylinder is printed before the cube, the ink will be trapped in the hole, preventing the cylinder material from being introduced. It also showcases the interference caused by tessellation between layers of different materials, resolved by morphological erosion.

(ii) A cube composed of two interlocking pieces made of different materials (Figure 6B). The protruding part of piece A is overlapped by the top of piece B, which is an example of the overlapping constraint.

Three approaches to layer sequencing are:

(i) Naïve sequencing: The layers are printed in order. In the worst case, if each layer has two materials, the process ensures that the material A of each layer is always printed before material B. Therefore, for a three-layer and two-material model, the sequence is A–B–A–B–A–B. The number of material changes required is $L \times M - 1$, where L is the number of layers, and M is the number of materials.

(ii) Alternating naïve sequencing: The layers are printed in order, and the order of materials is inverted in each subsequent layer. Therefore, for a three-layer and two-material model, the sequence is A–A–B–B–A–A. This saves one material change with respect to the previous naïve method, as the first material fabricated in a new layer is the same as the last material in the previous layer. The number of changes required for a two-material object is equal to the total number of layers, approximately half that of naïve sequencing.

(iii) Our method: The algorithm described in **Section 2.4** minimizes the number of changes while satisfying the overlapping and trapping constraints (Table 1).

Table 1. Comparison of the material changes required for our method

Model	Number of material changes		
	Naïve sequence (A–B–A–B–A–B)	Alternating naïve sequence (A–A–B–B–A–A)	Our method
Interlocked cube	99	50	2
Cube with cylinder	99	50	1

3.2. Printing validation

The first test involved printing the interlocked cube. Figure 7A illustrates a section of the part where the overlapping layers are easily identifiable, corresponding to the referenced issue. The planned process proceeds as follows: it begins with material B, printing layers 1–34 in sequence. After that, a cleaning step with Milli-Q water starts to remove excess non-crosslinking material and prevent cross-contamination between the materials. Then, it switches to material A, printing all layers (1–50) without interruption, followed by another cleaning step. Finally, it returns to material B to print the remaining layers (35–50). In this case, using the developed algorithm optimized the material change, requiring only two material switches instead of 50. Figure 7A shows the structure printed using the proposed algorithm in a continuous printing process, alongside the same structure printed by fabricating each material separately and then manually assembling them. As can be seen, the resulting model exhibited perfect integration between the two materials, as they were printed *in situ*. In contrast, the manually assembled structure showed clear separations between the materials, as indicated by the arrows. The sub-part, composed of either material B or material A, was completed according to the sequence determined by the algorithm.

The second object that was printed was a cube with an internal cylinder (Figure 7B). This object encompasses the two issues discussed above: interference caused by tessellation between layers of different materials and trapped ink. The first issue was effectively resolved using growth and shrinkage techniques. The printing process began with layers of the blue material, spreading around the base of the cylinder. Once finished, the ink was washed, and the vat was changed to print the entire second material. In this case, the developed algorithm optimized the material change to only one instead of 50 changes. Figure 7B compares structures printed via the continuous process and those manually assembled. Once again, the manually assembled structures displayed noticeable gaps (highlighted by arrows), whereas the continuous printing process produced a homogeneous structure with superior integration.

As an additional qualitative validation, a yin–yang model composed of two materials was printed to verify the accuracy of material boundary definition and the effectiveness of the cleaning process between consecutive material changes (Figure 7C). This simple yet illustrative geometry demonstrated a clear separation between materials, confirming the proper functioning of the multimaterial workflow.

To further quantitatively assess the efficiency of the proposed printing algorithm, additional structures with more than two materials were fabricated and analyzed. In these tests, the number of material changes required using the optimized algorithm was compared against a conventional layer-by-layer multimaterial printing method. Structures such as those presented in Figure 7D & E were printed and evaluated to quantify the optimization achieved in material switching.

The results, as summarized in Table 2, showed a substantial reduction in the total number of material changes when using the proposed algorithm, confirming its scalability and effectiveness for multimaterial printing beyond two-material configurations.

Additionally, the printing method was validated using a DNA-like helix structure to demonstrate its applicability for geometries that cannot be printed separately and later assembled. Figure 7F shows the printed structure from lateral and top views, where the material transitions and the perfect integration between them are clearly visible.

To optimize the fabrication of PEGDA-based scaffolds via photopolymerization, we systematically tuned printing parameters, with a particular focus on pore architecture and optical resolution (Figure 8). Scaffolds with gap sizes of 200 μm (Figure 8A), 400 μm (Figure 8B), and 600 μm (Figure 8C) were printed to evaluate the impact of feature dimensions on resolution fidelity and structural integrity. To mitigate light scattering and reduce *out-of-focus* crosslinking, 0.025% w/v tartrazine was incorporated as a photoabsorber.[23] This incorporation effectively quenched excess light penetration beyond the intended voxel boundary, improving *z*-axis resolution and enabling sharper feature definition. The combined optimization of gap size and photopolymer composition allowed for enhanced control over scaffold geometry, which is critical for tissue engineering applications.[24]

Table 2. Reduction in the total number of material changes when using the proposed algorithm

Model	Number of materials	Layers	Material switches (conventional layer-by-layer)	Material switches (optimized algorithm)
"Traffic light"	4	50	81	4
"Yin–yang"	2	20	40	2
"Yin Yan Yun"	3	20	60	3

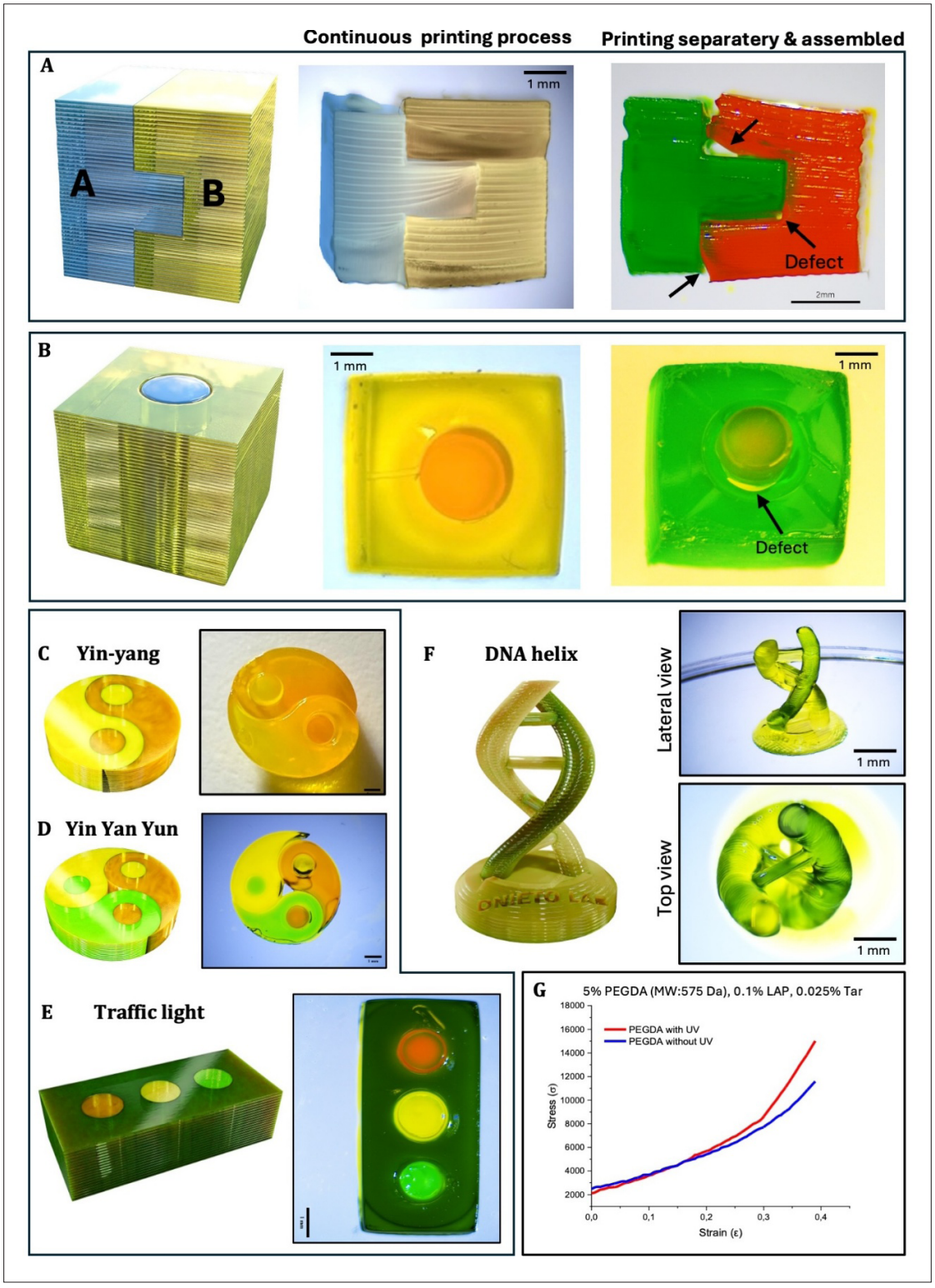

Figure 7. Multimaterial DLP bioprinting of complex structures and mechanical characterization. (A & B) Objects composed of subcomponents with shared layers, illustrating the contrast between a continuous multimaterial printing process and printing the components separately, followed by manual assembly. (C–F) Examples of multimaterial printed objects highlighting the capabilities of the bioprinter: (C) yin–yang design, (D) Yin Yan Yun variation, (E) traffic light model, and (F) DNA-like helix structure. (G) Stiffness measurements of printed objects before and after post-printing UV exposure. Abbreviations: LAP: lithium phenyl-2,4,6-trimethylbenzoylphosphinate; MW: molecular weight; PEGDA: poly(ethylene glycol) diacrylate; Tar: tartrazine.

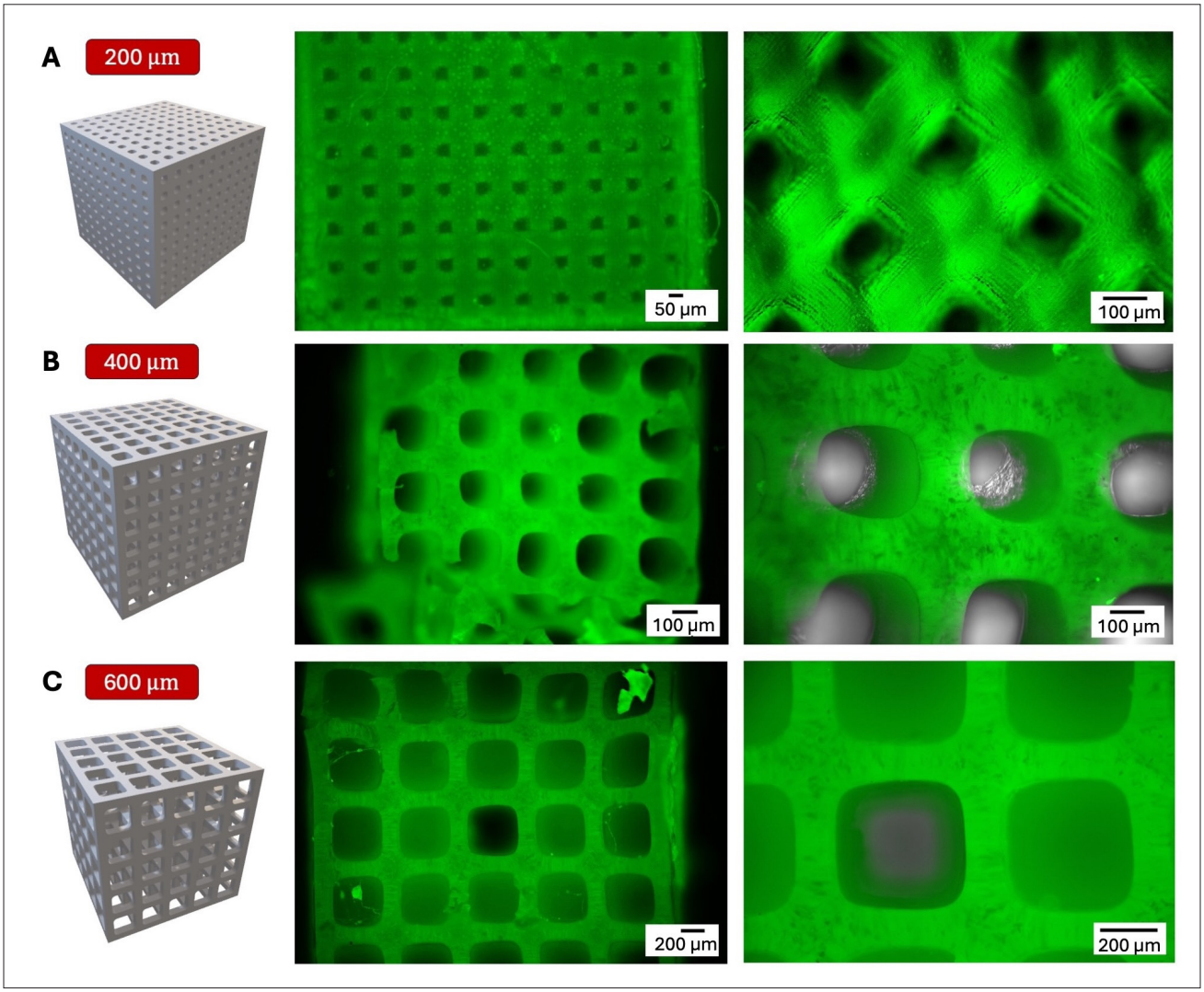

Figure 8. Microscopy images of the bioprinted scaffolds with various dimensions: (A) 200 µm (scale bars: 50 µm [left], 100 µm [right]; magnifications: 4× [left], 10× [right]), (B) 400 µm (scale bar: 100 µm; magnifications: 4× [left], 10× [right]), and (C) 600 µm (scale bar: 200 µm; magnifications: 4× [left], 10× [right]).

To enhance the mechanical properties of PEGDA hydrogels, we applied a high-irradiance post-curing step intended to increase the strain tolerance of the material. This additional curing phase promotes further crosslinking within the polymer network, potentially leading to improved structural integrity.[25] Apparent compressive modulus and equilibrium Q_M were measured on PEGDA disks with and without the 60-s high-irradiance post-cure to evaluate the impact of post-curing on both mechanical stiffness and swelling behavior (Figure 7D).

In addition to material optimization, the structural fidelity of these lattice scaffolds is not solely dependent on material composition, but is also intrinsically linked to the slicing strategy. Unlike standard geometric slicing, which can introduce artifacts or erroneous overlaps at fine strut intersections, our voxel-based approach employs morphological erosion to eliminate these interferences prior to projection. This computational correction ensures that pore geometries remain open and well-defined, effectively translating the digital design into the physical object without the pore closure often observed in conventional workflows.

3.3. Relationship between light exposure and material crosslinking

Apparent compressive modulus and equilibrium Q_M were measured on PEGDA disks with and without the 60-s high-irradiance post-cure (Table 3).

Swelling tests provide an estimate of the crosslink density of the materials: a lower crosslink density generally

Table 3. Apparent compressive modulus and equilibrium swelling ratio (Q_M)

Material	Post-cure	Apparent elastic modulus (kPa)	Q_M
PEGDA (5% w/v, MW = 575 Da)	No	12.36 ± 0.66	14.45 ± 3.10
PEGDA (5% w/v, MW = 575 Da)	Yes	14.34 ± 1.40	13.05 ± 2.18

Abbreviations: MW: molecular weight; PEGDA: poly(ethylene glycol) diacrylate.

allows for greater swelling (a higher Q_M), while a highly crosslinked network produces less swelling.[26] In our PEGDA builds, post-curing modestly reduced the Q_M, while the apparent elastic modulus increased slightly (Figure 7D). These trends indicate a slight densification of the network; however, the similarity of the moduli before and after post-curing suggests that the layer exposures used during printing already produced a highly converted PEGDA network.

3.4. Cell viability

To assess the bioprinting capabilities, a multimaterial cube scaffold loaded with H9c2 cardiomyoblasts was successfully fabricated (Figure 9). Live/Dead staining revealed consistently high levels of cell survival across all evaluated time points. The quantitative analysis of viability (Figure 9E) at days 1, 3, and 5 showed no significant differences among groups, indicating that cell viability remained stable throughout the culture period, as expected due to the cell adhesion properties and excellent biocompatibility of GelMA.[27,28]

3.5. Comparison of theoretical vs. printing process

This work presents a novel algorithm to address the aforementioned challenges by generating an optimized set of printing layers that minimizes the number of required cleaning cycles. Theoretical predictions from the sequencing algorithm were validated through multimaterial printing of the two test models: the interlocked cube and the cube containing an internal cylinder. In both cases, the algorithm successfully minimized material changes while satisfying critical constraints, including layer overlapping and ink trapping. For the interlocked cube, the theoretical sequence (printing layers 1–34 of material B, followed by all layers of material A, and then returning to material B for layers 35–50) was implemented experimentally, resulting in only two material changes compared to 50 required by alternating naïve sequencing. The printed structure (Figure 7A) closely matched the intended design, with clear resolution of overlapping features. Similarly, the internal cylinder model demonstrated the algorithm's effectiveness in avoiding ink trapping by printing the cylinder (material B) entirely before enclosing it with the cube (material A), requiring only a single material change instead of 50. The experimental print (Figure 7B) confirmed the theoretical model's accuracy, with successful resolution of tessellation artifacts through morphological operations and correct material sequencing. Together, these results confirm that the theoretical sequencing model translates reliably to physical prints, optimizing both process efficiency and structural fidelity. Three approaches to layer sequencing are compared in Table 1.

4. Conclusion

This work presents a novel slicing system for optimizing multimaterial bioprinting using a top–down DLP printer. The proposed algorithm addresses key challenges such as layer overlapping and tessellation artifacts that arise when multiple materials are present within the same layer. Our approach operates at a hardware-oriented level by applying morphological operations directly to the bitmap images sent to the digital micromirror device. This low-level image processing strategy aligns natively with the projector's pixel-level functioning, ensuring high geometric fidelity throughout the print.

To optimize printing performance, the algorithm is designed to minimize the number of material changes during fabrication. This reduces the risk of cross-material interference in subsequent layers and shortens overall printing time without compromising print quality or resolution. Importantly, the system also mitigates ink retention issues that occur during the lamination process, especially in scenarios where one material is fully enclosed by another.

We validated the system both theoretically and experimentally using test models and a complex multimaterial, cell-laden microenvironment. The implementation of morphological and advanced image processing operations enables high parallelization on modern GPUs, making the computational pipeline highly efficient and scalable. This allows for the rapid handling of complex models with numerous layers or intricate morphologies.

Experimental results demonstrated improved print fidelity, reduced processing time, and enhanced material resolution. We further highlighted the practical utility of our system by fabricating a multimaterial tissue construct consisting of a PEGDA-based structural scaffold integrated with a GelMA-based, cell-laden microenvironment.

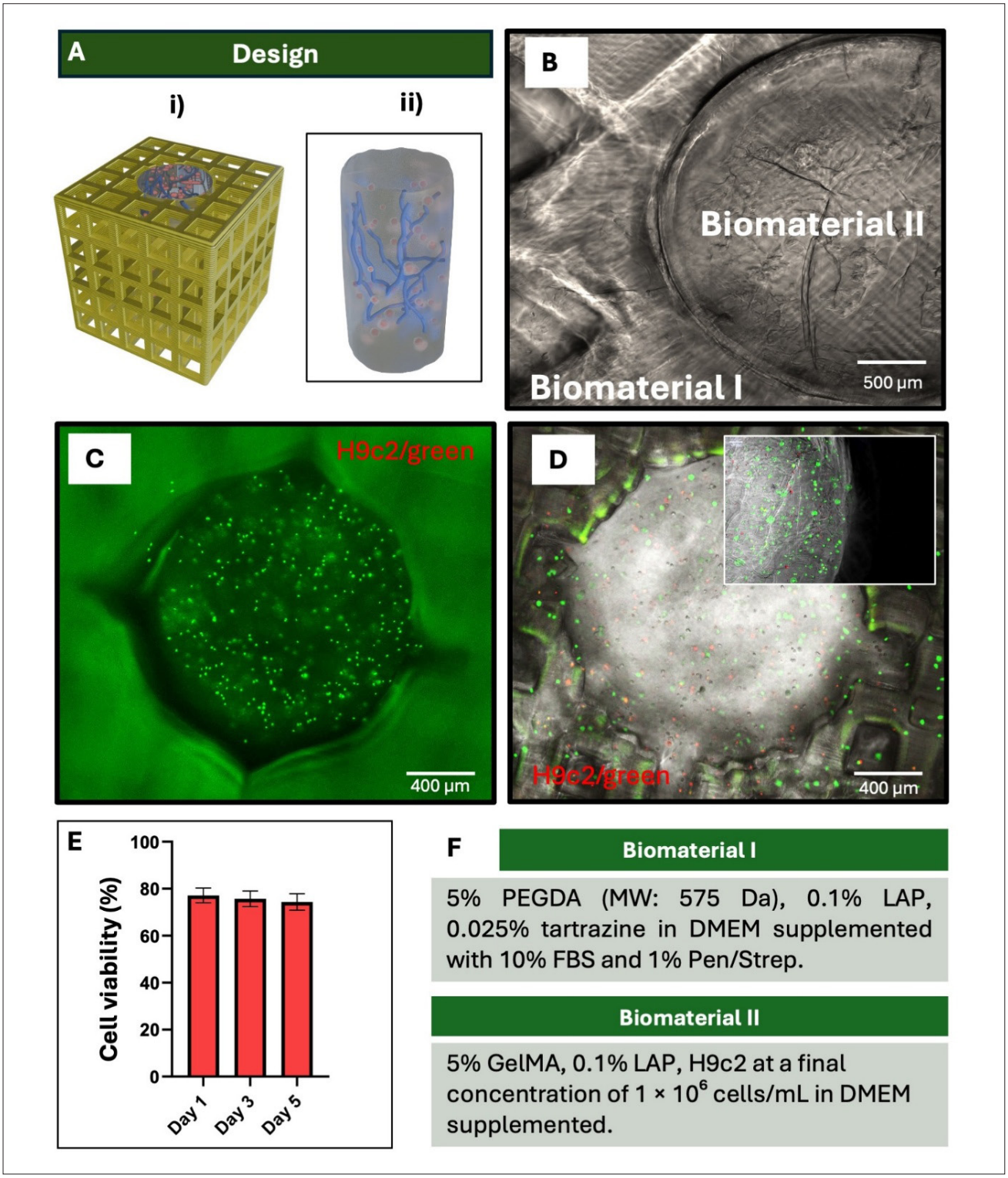

Figure 9. Multimaterial cell-laden scaffold bioprinting and in vitro cell viability assessment. (A) Design of the two-material cell-laden scaffolds. (B) Microscope image of a two-material printed scaffold (scale bar: 500 µm; magnification: 20×). (C) Microscope image of a multimaterial scaffold embedded with H9c2 cells (scale bar: 400 µm; magnification: 10×). (D) Image of live/dead assay results. The inset shows H9c2 cells seeded on the scaffolds after 24 h of culture (scale bars: 400 µm, magnifications: 10X µm [inset]; magnifications: YYY, YYY [inset]). (E) Cell viability. (F) Composition of the two materials used. Abbreviations: DMEM: Dulbecco's modified Eagle medium; FBS: fetal bovine serum; GelMA: gelatin methacryloyl; LAP: lithium phenyl-2,4,6-trimethylbenzoylphosphinate; MW: molecular weight; PEGDA: poly(ethylene glycol) diacrylate; Pen/Strep: penicillin/streptomycin.

Acknowledgments

None

Funding

Alejandro González-Santos was supported by a predoctoral research grant from the Xunta de Galicia (Consellería de Cultura, Educación, Formación Profesional e Universidades). This grant was co-funded by the European Union (FSE+ Galicia 2021-2027). Daniel Nieto was funded by the European Research Council Consolidator Grant (101125172 HOT-BIOPRINTING- HE-ERC-2023COG) and was supported by the Oportunius Programme (Xunta de Galicia) since 2024.

Conflict of interest

The authors declare that they have no conflict of interest.

Author contributions

Conceptualization: Julián Flores, Daniel Nieto
Formal analysis: Alejandro González-Santos, Nadina Usseglio
Investigation: Alejandro González-Santos, Adrian García, Nadina Usseglio
Methodology: Alejandro González-Santos, Adrian García, Julián Flores, Daniel Nieto
Supervision: Julián Flores, Daniel Nieto
Writing – original draft: Julián Flores, Daniel Nieto
Writing – review & editing: Alejandro González-Santos, Nadina Usseglio, Julián Flores, Daniel Nieto

Ethics approval and consent to participate

Not applicable.

Consent for publication

Not applicable.

Availability of data

The authors declare that the data supporting the findings of this study are available within the paper. Should any raw data files be needed in another format, they are available from the corresponding author upon reasonable request.

References

1. Deo KA, Singh KA, Peak CW, Alge DL, Gaharwar AK. Bioprinting 101: design, fabrication, and evaluation of cell-laden 3D bioprinted scaffolds. *Tissue Eng Part A*. 2020;26(5-6):318-338.
doi: 10.1089/ten.tea.2019.0298

2. Tripathi S, Mandal SS, Bauri S, Maiti P. 3D bioprinting and its innovative approach for biomedical applications. *MedComm (2020)*. 2023;4(1):e194.
doi: 10.1002/mco2.194

3. Mirshafiei M, Rashedi H, Yazdian F, Rahdar A, Baino F. Advancements in tissue and organ 3D bioprinting: current techniques, applications, and future perspectives. *Mater Des*. 2024;240:112853.
doi: 10.1016/j.matdes.2024.112853

4. Leberfinger AN, Dinda S, Wu Y, *et al*. Bioprinting functional tissues. *Acta Biomater*. 2019;95:32-49.
doi: 10.1016/j.actbio.2019.01.009

5. Li W, Wang M, Ma H, Chapa-Villarreal FA, Lobo AO, Zhang YS. Stereolithography apparatus and digital light processing-based 3D bioprinting for tissue fabrication. *iScience*. 2023;26(2):106039.
doi: 10.1016/j.isci.2023.106039

6. Alparslan C, Bayraktar Ş. Advances in digital light processing (DLP) bioprinting: a review of biomaterials and its applications, innovations, challenges, and future perspectives. *Polymers (Basel)*. 2025;17(9):1287.
doi: 10.3390/polym17091287

7. Nazir A, Gokcekaya O, Md Masum Billah K, *et al*. Multi-material additive manufacturing: a systematic review of design, properties, applications, challenges, and 3D printing of materials and cellular metamaterials. *Mater Des*. 2023;226:111661.
doi: 10.1016/j.matdes.2023.111661

8. Kwok TH. Comparing slicing technologies for digital light processing printing. *J Comput Inf Sci Eng*. 2019;19(4):044502.
doi: 10.1115/1.4043672

9. Yang S, Wang L, Chen Q, Xu M. In situ process monitoring and automated multi-parameter evaluation using optical coherence tomography during extrusion-based bioprinting. *Addit Manuf*. 2021;47:102251.
doi: 10.1016/j.addma.2021.102251

10. Kim H, Choi J, Wicker R. Scheduling and process planning for multiple material stereolithography. *Rapid Prototyp J*. 2010;16(4):232-240.
doi: 10.1108/13552541011049243

11. Shaukat U, Rossegger E, Schlögl S. A review of multi-material 3D printing of functional materials via vat photopolymerization. *Polymers (Basel)*. 2022;14(12):2449.
doi: 10.3390/polym14122449

12. Shaukat U, Thalhamer A, Rossegger E, Schlögl S. Dual-vat photopolymerization 3D printing of vitrimers. *Addit Manuf*. 2024;79:103930.
doi: 10.1016/j.addma.2023.103930

13. Chin KCH, Ovsepyan G, Boydston AJ. Multi-color dual wavelength vat photopolymerization 3D printing via spatially controlled acidity. *Nat Commun*. 2024;15(1):3867.
doi: 10.1038/s41467-024-48159-7

14. Ghaderi I, Behravesh AH, Hedayati SK, *et al*. Multimaterial additive manufacturing of poly-L-lactic acid–hydroxylapatite/graphene oxide scaffold fabricated via vat photopolymerization: experimental investigation, analysis and cell study. *Rapid Prototyp J*. 2024;30(9): 1789-1802.
doi: 10.1108/RPJ-02-2024-0085

15. Preparata FP, Shamos MI. *Computational Geometry*. New York: Springer; 1985.
doi: 10.1007/978-1-4612-1098-6

16. Keeter M. DLP Slicer. https://www.mattkeeter.com/projects/dlp

17. Shreiner D, Sellers G, Kessenich JM, Licea-Kane BM. *OpenGL Programming Guide: The Official Guide to Learning OpenGL, Version 4.3*. Massachusetts, United States: Addison Wesley; 2013:984.

18. Gonzalez RC, Woods RE. *Digital Image Processing*. Harlow Essex, England: Pearson Education; 2018.

19. Choi YJ, Park H, Ha DH, Yun HS, Yi HG, Lee H. 3D bioprinting of in vitro models using hydrogel-based bioinks. *Polymers (Basel)*. 2021;13(3):366.
doi: 10.3390/polym13030366

20. Gao J, Li M, Cheng J, *et al*. 3D-printed GelMA/PEGDA/F127DA scaffolds for bone regeneration. *J Funct Biomater*. 2023;14(2):96.
doi: 10.3390/jfb14020096

21. Mancha Sánchez E, Gómez-Blanco JC, López Nieto E, *et al*. Hydrogels for bioprinting: a systematic review of hydrogels synthesis, bioprinting parameters, and bioprinted structures behavior. *Front Bioeng Biotechnol*. 2020;8:776.
doi: 10.3389/fbioe.2020.00776

22. Schneider CA, Rasband WS, Eliceiri KW. NIH Image to ImageJ: 25 years of image analysis. *Nat Methods*. 2012;9(7):671-675.
doi: 10.1038/nmeth.2089

23. Yang Y, Zhou Y, Lin X, Yang Q, Yang G. Printability of external and internal structures based on digital light processing 3D printing technique. *Pharmaceutics*. 2020;12(3):207.
doi: 10.3390/pharmaceutics12030207

24. Flores-Jiménez MS, Garcia-Gonzalez A, Fuentes-Aguilar RQ. Review on porous scaffolds generation process: a tissue engineering approach. *ACS Appl Bio Mater*. 2023; 6(1):1-23.
doi: 10.1021/acsabm.2c00740

25. Şener Raman T, Kuehnert M, Daikos O, *et al*. A study on the material properties of novel PEGDA/gelatin hybrid hydrogels polymerized by electron beam irradiation. *Front Chem*. 2023;10:1094981.
doi: 10.3389/fchem.2022.1094981

26. Metz J, Gonnerman K, Chu A, Chu TMG. Effect of crosslinking density on swelling and mechanical properties of PEGDA400/PCLTMA900 hydrogels. *Biomed Sci Instrum*. 2006;42:389-394.

27. Bupphathong S, Quiroz C, Huang W, Chung PF, Tao HY, Lin CH. Gelatin methacrylate hydrogel for tissue engineering applications—a review on material modifications. *Pharmaceuticals*. 2022;15(2):171.
doi: 10.3390/ph15020171

28. Fowler M, Moreno Lozano A, Krause J, *et al*. Guiding vascular infiltration through architected GelMA/PEGDA hydrogels: an *in vivo* study of channel diameter, length, and complexity. *Biomater Sci*. 2025;13(11):2951-2960.
doi: 10.1039/D5BM00193E